



Hi-C embedded polymer model of *Escherichia coli* reveals the origin of heterogeneous subdiffusion in chromosomal loci

Palash Bera, Abdul Wasim, and Jagannath Mondal ^{*}
Tata Institute of Fundamental Research, Hyderabad 500046, India

 (Received 29 October 2021; revised 5 May 2022; accepted 10 May 2022; published 2 June 2022)

Underneath its apparently simple architecture, the circular chromosome of *Escherichia coli* is known for displaying complex dynamics in its cytoplasm, with past investigations hinting at inherently diverse mobilities of chromosomal loci across the genome. To decipher its origin, we simulate the dynamics of genome-wide spectrum of *E. coli* chromosomal loci, via integrating its experimentally derived Hi-C interaction matrix within a polymer-based model. Our analysis demonstrates that, while the dynamics of the chromosome is subdiffusive in a viscoelastic media, the diffusion constants are strongly dependent of chromosomal loci coordinates and diffusive exponents (α) are widely heterogenous with $\alpha \approx 0.36$ – 0.60 . The loci-dependent heterogeneous dynamics and mean first-passage times of interloci encounter were found to be modulated via genetically distant interloci communications and is robust even in the presence of active, ATP-dependent noises. Control investigations reveal that the absence of Hi-C-derived interactions in the model would have abolished the traits of heterogeneous loci diffusion, underscoring the key role of loci-specific genetically distant interaction in modulating the underlying heterogeneity of the loci diffusion.

DOI: [10.1103/PhysRevE.105.064402](https://doi.org/10.1103/PhysRevE.105.064402)

I. INTRODUCTION

The chromosome of the prototypical bacteria *Escherichia coli* consists of 1.6 mm super-coiled circular DNA of 4.64 Mb. Unlike eukaryotes, it has no nucleus and it is confined within a (2–4) μm long spherocylinder [1,2]. However, the perception that bacterial chromosome is a randomly packed DNA, is fast changing. Precedent investigations have provided numerous evidences that the “nucleoid” is just not a complex blob of genomic DNA, RNA, and associated proteins. Rather it is being replaced by a picture of self-organized architecture with distinctly segregated macrodomains (MDs) and nonstructured (NS) regions [3,4]. In addition to traditional molecular biology-based experiments [3–9], the emergence of Chromosome conformation capture techniques in bacteria [10–12] are providing a microscopic view of the genome-level organization of its chromosome. In particular, a high resolution (5 kb), Hi-C contact map for *E. coli* has recently been reported by Lioy *et al.* [13]. The subsequent integration of this Hi-C-derived interaction map in a polymer-based computational model [14], had bestowed a clear chromosomal compartmentalization, a fundamental building block of *E. coli* chromosomal architecture. In light of this, the center of our current investigation is the following: How does the self-organised nature of the *E. coli* chromosome impact the dynamics of its individual loci?

The dynamics of chromosomal loci is generally quantified by mean-squared displacements (MSD). Generally, for a diffusive particle $\text{MSD} \sim \tau^\alpha$, where τ is lag time and α is called MSD exponent. $\alpha = 1$ indicates normal diffusion

[15,16], $\alpha > 1$ indicates super-diffusion [17–20] and $\alpha < 1$ implies subdiffusion. Previous interesting experimental and theoretical investigations by Weber *et al.* [21–24] and Javer *et al.* [25] mainly focused on the spatiotemporal dynamics of *E. coli* chromosomal loci. Weber *et al.* explored the dynamics of chromosomal loci in a time interval between 1 and 100 s in LB medium (wt37LB). Their investigations showed that the movement of individual loci is subdiffusive with a universal diffusive exponent $\alpha = 0.39$ and this value was reported by them to be robust for both *E. coli* and *Caulobacter crescentus* with different drug treatments. A key conclusion of the investigations by Weber *et al.* [21,22] was that this universal value cannot be explained by typical Rouse-like polymer model [26,27]. Their measurement of velocity autocorrelation function with a negative peak indicated a viscoelastic nature of cytoplasm. A subsequent study by the same group had shown that ATP dependent biological activities do not change these robustness of MSD exponent but mobility of loci changes significantly [24]. However, in a later crucial investigation, Javer *et al.* [25] had investigated the dynamics of a large set of chromosomal loci across the genome within very short timescale (0.1–10 s) in minimal medium, using high resolution tracking method. While this investigation also found that the MSD exponents of all loci indicate a subdiffusive motion even in short time, there is a large variation of mobility across the chromosome loci. More importantly, the diffusivity of Ter macrodomain was found to be very low compared to other macrodomains. Together, these investigations bring out the complexity in the dynamics of the *E. coli* chromosome and allude to a heterogeneous loci dependence. However, a microscopic picture of the origin of such observations are yet to emerge, especially at individual chromosome loci level.

*jmondal@tifrh.res.in

Based on these precedent investigations and particularly the observation of the heterogeneous diffusivity across the loci, we surmised that the interloci cross-talk and specific identity of loci pair might play an important role. There have been multiple previous modeling attempts [28–36] but the present work is the first attempt to explore and explain the loci-dependent diffusivities using a Hi-C integrated model. Toward this end, we planned on employing our recent model of *E. coli* chromosome [14], which had integrated the high-resolution (5 kb) Hi-C interaction map [13] in an excluded-volume polymer-based framework, for investigating the dynamics of the chromosomal loci. Specifically we use this Hi-C-encoded model to explore the mobility of each of 30 loci (same set of loci as investigated by Javer *et al.*'s tracking experiments) via Brownian dynamics (BD) simulations. Our analysis of the simulation trajectories reveal that both the diffusion constant and the exponents are loci-coordinate dependent and indicate a heterogeneous distribution. The result is found to be robust in presence of active noise. Interestingly, our control simulations via turning off the Hi-C-derived interactions in the model abolishes this heterogeneity, suggesting that the loci-specific intergene interactions, as encoded in the Hi-C map, hold the key to the complex dynamics of the bacterial chromosome.

II. MODEL AND METHODS

A. Model details

In Hi-C measurement, the cells are in an ensemble of different replication stages with their respective cell cycles. Here we are interested in short-time chromosomal loci dynamics in minimal medium (wt30MM), i.e., there is only one single chromosome and no replication fork. We model the *E. coli* chromosome as a bead-in-a-spring polymer chain, with each bead representing 5×10^3 bp (5 kb), the same as our previous work [14] which provides the details of the modeling aspect. Here we provide essential features of the model. The resolution of the model is the same as Hi-C interaction maps reported by Lioy *et al.* [13]. To mimic the confinement in the *E. coli* cell, we have taken the polymer chain in a spherocylindrical confinement with average length $L = 3.08 \mu\text{m}$ (including two end caps) and diameter $d = 0.82 \mu\text{m}$. By taking approximate volume fraction of chromosome $f_r = 0.1$ [37], we have calculated the bead diameter σ to be $0.06731 \mu\text{m}$ (see Supplemental Material [38]). Nonbonded interactions of the polymer beads are modeled by the repulsive part of Lenard Jones (LJ) potential i.e., $V_{\text{nb}}(r) = 4\epsilon(\sigma/r)^{12}$ (where ϵ is in the unit of $k_B T$ and r is in the unit of σ). Bonded interactions between adjacent beads have been modeled by harmonic springs with a spring constant $k_{\text{spring}} = 300k_B T/\sigma^2$. In a similar fashion, Hi-C contacts are also modeled as harmonic springs with distance dependent force constants and probability dependent bond lengths.

From the Hi-C contact probability matrix we can calculate the distance matrix D as Eq. (1):

$$D_{ij} = \sigma/P_{ij}, \quad (1)$$

where i and j are row and column index of the matrix, respectively. From this distance matrix we define a restraining potential between a pair of Hi-C contacts at a separation of

r_{ij} , as $V_{\text{Hi-C}}(r_{ij}) = \frac{1}{2}k_{ij}(D_{ij} - r_{ij})^2$. Here k_{ij} is a distance-dependent force constant that can be calculated from Eq. (2):

$$k_{ij} = k_0 e^{-\frac{(D_{ij}-\sigma)^2}{w^2}}. \quad (2)$$

This relation implies that the force constant becomes smaller for larger distances and the k_0 value is the upper bound of the force constant. We have used a value of $k_0 = 10k_B T/\sigma^2$ [14]. For optimization of w we have calculated the Pearson Correlation coefficient between the experimental and simulated contact probability matrices with varying w^2 . Pearson correlation coefficient values show a maximum (88%) at $w^2 = 0.3$. Nonetheless, as would be revealed afterwards, we have also varied the value of k_0 to ascertain the robustness or trend of observed results. For the spherocylindrical confinement mimicking the cell wall, we have used a restraining potential in the form of Eq. (3):

$$V_{\text{res}}(r; R_0) = \frac{1}{2}k_{\text{res}}|\vec{r} - \vec{R}_0|^2 \mathbf{H}(|\vec{r} - \vec{R}_0|). \quad (3)$$

Here R_0 is the center of the spherocylindrical confinement and k_{res} is the force constant depicting the relative ‘‘softness’’ of the confinement. We have used a value of $k_{\text{res}} = 310k_B T/\sigma^2$. \mathbf{H} is a step function that will activate if a polymer bead gets out from the spherocylindrical confinement. Therefore, the Hamiltonian can be written as Eq. (4):

$$V_{\text{tot}} = V_b(r) + V_{\text{nb}}(r) + V_{\text{Hi-C}}(r_{ij}) + V_{\text{res}}(r; R_0), \quad (4)$$

where $V_b(r)$, $V_{\text{nb}}(r)$, $V_{\text{Hi-C}}(r_{ij})$, and $V_{\text{res}}(r; R_0)$ are bonded, nonbonded, Hi-C restraining, and confinement restraining potential, respectively.

We have also carried out control simulations with a set of variants of the present model. In particular, to investigate the effect of Hi-C-derived interactions, we have done separate simulations by switching off the Hi-C related terms [$V_{\text{Hi-C}}(r_{ij})$] from the model potential functions.

B. Simulation method details

To study the dynamics of chromosomal loci, here we have used Brownian dynamics (BD) simulations (overdamped condition), by integrating Eq. (5) (Euler scheme):

$$\frac{d\vec{r}_i}{dt} = -\frac{D_i}{k_B T} \vec{\nabla} V_{\text{tot}} + \vec{R}_i(t), \quad (5)$$

where D_i is diffusion coefficient of i th bead and $\vec{R}_i(t)$ is a random noise, satisfying fluctuation dissipation theorem, i.e., $\langle \vec{R}_i(t) \cdot \vec{R}_j(t') \rangle = 6D_i \delta_{ij} \delta(t - t')$. We can calculate D_i from the Stokes-Einstein equation $D_i = \frac{k_B T}{\gamma} = \frac{k_B T}{3\pi\eta\sigma}$, Where η is the *E. coli* cytosol viscosity and value is 17.5 Pa s [39,40]. Here all simulations time in the unit of $\tau_{\text{BD}} = \frac{\sigma^2}{D} \approx 12 \text{ s}$. Integration of the 5 was performed with a time step $\delta t = 1 \times 10^{-4} \tau_{\text{BD}}$ by setting $k_B T = 1$.

To simulate the effect of ATP-dependent active forces, we have done additional control simulations by modulating the BD simulation protocol such that random noise does not follow fluctuation-dissipation theorem. The fluctuation dissipation theorem has been changed to $\langle \vec{R}(t) \cdot \vec{R}(t') \rangle = 12D\delta(t - t')$ instead of the usual expression $\langle \vec{R}(t) \cdot \vec{R}(t') \rangle = 6D\delta(t - t')$. We have also systematically explored the trend of the dynamics by considering other values of noise strengths.

All simulations were performed using the open source package GROMACS 5.0.6 [41] and we have modified the source code to introduce the spherocylindrical confinement. For data analysis and visualization, we have used python libraries [42–46] and visual molecular dynamics (VMD) [47], respectively. We have taken 200 different initial configuration (ensemble) of the polymer chain and minimized the energy of topology by steepest descent algorithm. After energy minimization, we allow the chain for equilibrium with $1 \times 10^6 \tau_{BD}$ time steps. Then we collected the data with time step $1 \times 10^3 \tau_{BD}$ (data saving frequency).

As a central metric, the simulation trajectories have been utilised to compute the MSD of a set of thirty loci [25] across entire chromosome. The MSDs were analysed in details for extracting diffusive exponents and diffusion constants. The details of all analysis (including the MSDs) performed in the present work have been provided in the Supplemental Material [38].

III. RESULTS AND DISCUSSION

A. An integrative computer model recapitulates *E. coli*'s Hi-C contacts

The chromosome of *E. coli* grown in minimal media at 30°C (wt30MM) forms the basis of our investigation of the dynamics of its loci. Majority of the relevant experiments involving dynamics has also been performed on this growth condition. The cytoplasm of *E. coli* at this particular growth condition, contains a single chromosome, is not complicated by the fast replication process, and hence is devoid of replication forks. As a result, the chromosome serves as a prototypical system which can be investigated for its short-time dynamics (20 min in real physical unit), without worrying about the chromosome segregation. Toward this end, we implemented a computer model of the *E. coli* chromosome by integrating beads-spring polymer topology with recently reported Hi-C interactions matrix of *E. coli* [13] chromosome at this particular condition (wt30MM). For this purpose, we employ a recently proposed protocol by our group [14]. As detailed in the Sec. II, the excluded volume interaction, Hi-C contacts and a spherocylindrical confinement form the key interactions of the model. We generated an ensemble of dynamical trajectories of the time-evolution of the chromosome model via BD simulations under over-damped condition (see Sec. II). Figure 1(a) renders a representative snapshot of the chromosome with color-coded encircled beads referring to various loci for different macrodomains and various nonstructured regions, as obtained in the simulations. The segregation of chromosome into six key macrodomains, a signature feature of *E. coli*, is clearly evident. To assess the precision of the simulated model, we first compare the ensemble-averaged interbead contact probability with the experimental Hi-C matrix. Figures 1(b) and 1(c) depict the heat maps of experimental and simulated contact probability matrices. The occurrence of an intense diagonal in both experimentally derived and simulated matrices represents that there is a higher contact probability between the chromosomal region for lower distances. Figures 1(d) and 1(e) demonstrate the heat map difference between experimental and simulated contact

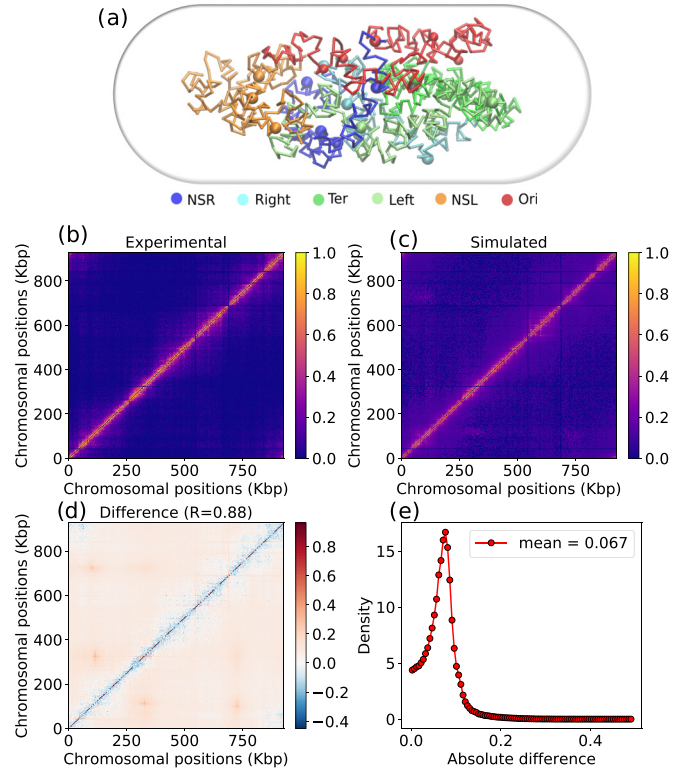


FIG. 1. (a) Snapshots of an equilibrated chromosome, taken from a particular trajectory. The different color-coded regions represent corresponding macrodomains (MD) and nonstructured (NS) regions and various colored beads encircled represent assorted loci for different MDs and NS regions. (b) Heat map of experimental Contact probability matrix. (c) Heat map of simulated contact probability matrix. This matrix is an ensemble average over 200 different initial configurations. (d) Heat map of difference matrix (simulated-experimental). R value is the Pearson correlation coefficient between simulated and experimental contact probability matrix values. (e) Histogram of absolute difference between simulated and experimental contact probability matrices with a mean of ~ 0.067 .

probability matrices and a histogram of this difference value, respectively. A Pearson correlation coefficient (PCC) value of 0.88 between experimental and simulated contact probability matrices and an absolute difference of the mean value of 0.067 between them imply reasonably good concurrence with *in vivo* and *in silico* chromosomal interactions.

To get better insight into the extent of agreement between simulated and experimental Hi-C matrices, we first removed diagonal (i, i) and nearby diagonal $(i + 1, i + 1; i - 1, i - 1)$ terms from the simulated and experimental Hi-C matrices, as these elements are contributing more and can potentially mask the contributions of other terms away from the diagonal. Then we calculated the PCC using the rest of the terms and plotted a linear fit between experimental and simulated contact probabilities (Fig. S1(a) in the Supplemental Material [38]). A PCC of $R = 0.90$ and slope of linear fit $m = 0.94$ provides a good concurrence between simulated and experimental Hi-C matrix. To get closer insight between these two Hi-C matrices, we divided these matrices into different MD

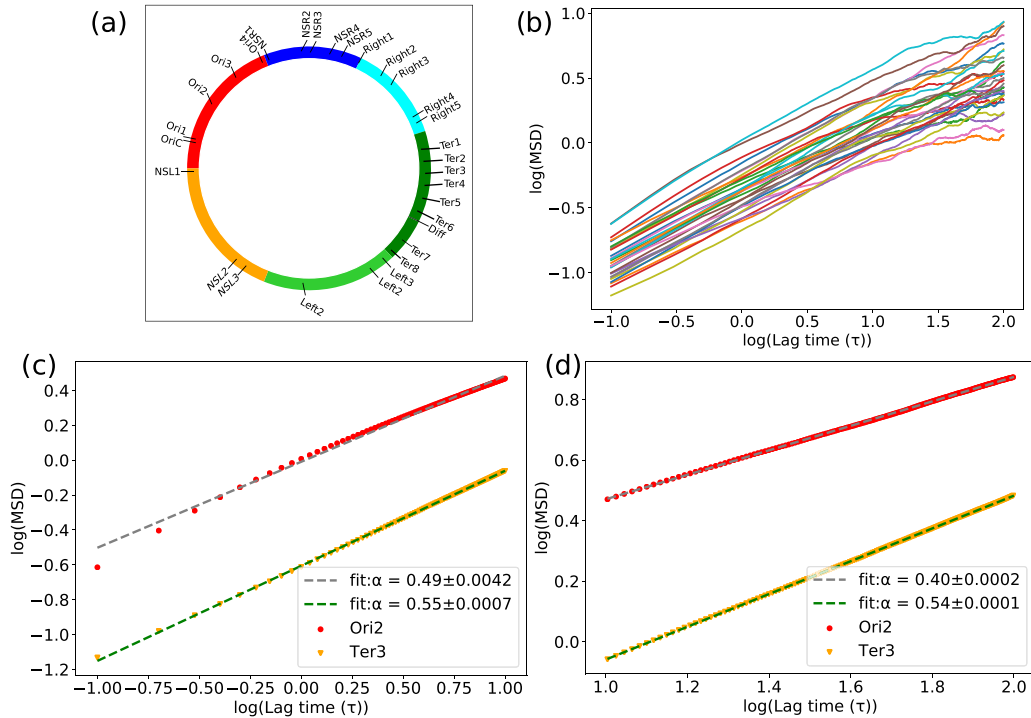


FIG. 2. (a) Different loci position in a circular chromosome according to their genomic coordinates. Different color chunks represent the macrodomains and nonstructured regions (NSR, NSL). (b) Time-averaged MSD from single trajectory as a function of lag time for different loci. (c) Power-law fitting of ensemble-average MSD for two loci (Ori2 and Ter3) with time lag $(0.1-10)\tau_{BD}$. Scatter points (red for Ori2 and orange for Ter3) are simulated data and dotted lines (gray fit for Ori2 and green fit for Ter3) are fitted data. Ori2 and Ter3 have subdiffusive exponents 0.49 ± 0.0042 and 0.55 ± 0.0007 , respectively. (d) Power-law fitting same as panel (c), with a lag time of $(10-100)\tau_{BD}$. Here Ori2 and Ter3 have MSD exponent 0.40 ± 0.0002 and 0.54 ± 0.0001 , respectively, less than as mentioned in panel (c). For all the plots MSD and time are in units of σ^2 and τ_{BD} , respectively, and these are in log scale.

segments (NSR-NSR, NSR-Right, NSR-Ter, Right-Ter, etc.) in accordance with their genomic coordinate and calculated the PCC between experimental and simulated Hi-C submatrices. Figure S1(b) in the Supplemental Material [38] represents the experimental Hi-C matrix and the PCC of the different segments with the simulated Hi-C matrix are highlighted in each of them. From this figure, it is clear that the PCC of the MDs and nearby MDs are relatively high compared to the far MDs region. A close look at Fig. S1(a) in the Supplemental Material [38] reveals small deviations in high and low contact probability in simulated matrix relative to the experimental one. We believe that these deviations appear mainly due to the confinement and the repulsive nature of the interbead interaction. In the present model, the contact probability (P_{ij}) is computed by calculating the distance (D_{ij}) between two beads and then converting them to probability as $P_{ij} = \sigma/D_{ij}$. Since in the current model, the maximum distance between any two pairs, separated by significantly large contour length, is bounded by the total length of the confinement, there is always a low but nonzero contact probability for two such bead pairs, which are otherwise lower or zero in the experimentally processed Hi-C interaction map. As a result, the current model slightly overestimates those low contact probabilities due to this spherocylindrical confinement. However, due to the current resolution (5 kbp) of the model and the interbead excluded volume interaction of the polymers being modeled via purely repulsive interaction, the model system-

atically overestimates the hardness of each of the polymer beads. This leads to inherent repulsion even among the beads that are close-by along the contour of the polymer. A higher repulsion in turn tends to place these beads a bit farther away than they should be in cellular environment (where other attractive interactions are possibly present), causing slightly lower contact probabilities along the diagonal of the simulated matrix when compared to the experimental contact probability matrix.

B. Loci mobility and diffusive exponents are chromosome coordinate dependent

Figure 2(a) shows the genomic position of different loci in the circular chromosome [3,4,25]. Each of the color segments in Fig. 2(a) represents an individual macrodomain and nonstructured region (NSR, NSL). Every macrodomain and nonstructured region contains its own corresponding loci position, giving rise to a total number of 30 loci. To study the dynamics of chromosomal loci, here we have used BD simulations in over-damped condition with a time step $\delta t = 1 \times 10^{-4} \tau_{BD}$. We simulate a time-range of $(0.1-100)\tau_{BD}$, which corresponds to (1.2 s–20 min) (significantly shorter than the doubling time of the bacteria at 30°C in MM). First we have calculated the time-averaged MSD for each trajectory (total 200 initial configurations) and subsequently have performed an average over all the trajectories, which

we define as “ensemble-average” ($\overline{\text{MSD}}_n$). The time profiles of MSD and the MSD exponents enable us to characterize the type of diffusion i.e., how fast the particles are spreading in space. The time-average MSD for a particular loci (n) defined as $(\text{MSD})_n(\tau) = \langle |\bar{r}_n(t + \tau) - \bar{r}_n(t)|^2 \rangle_t = \frac{1}{T_{\text{tot}}} \sum_t |\bar{r}_n(t + \tau) - \bar{r}_n(t)|^2$, where τ and T_{tot} are lag time and total simulation time, respectively. For a more appropriate power-law fitting of the ensemble-average MSD, we have used $(\overline{\text{MSD}}_n) = D\tau^\alpha$, D is constant). Generally, $(\overline{\text{MSD}}_n) = 6D_{\text{app}}\tau^\alpha$ (in 3D), D_{app} is the apparent diffusion coefficient, so we denote $D = 6D_{\text{app}}$ and α is the MSD exponent. We have divided the lag time into two regions: $(0.1-10)\tau_{\text{BD}}$ and $(10-100)\tau_{\text{BD}}$. We have also cross-checked that instead of the whole time lag, power-law fitting is better in these two divided regions.

Figure 2(b) demonstrates the time-averaged MSD, from a single trajectory as a function of lag time for different loci. The figure shows that there is a large spread in the time profiles of MSD across all loci. We first focus our attention on mobilities of two particular loci (Ori2, Ter3). Specifically, Figures 2(c) and 2(d) compare the ensemble-averaged MSD ($\overline{\text{MSD}}$) and its power-law fitting for these two particular loci (Ori2, Ter3) at $(0.1-10)\tau_{\text{BD}}$ and $(10-100)\tau_{\text{BD}}$, respectively. In these two figures the scatter points are simulated data and the dotted lines are fitted data. From these figures, it is evident that there is a significant difference in individual mobility between Ori2 and Ter3 loci. More importantly, the individual power-law fitting of the MSD profiles of these two loci reveal that the diffusive exponent is significantly lower than 1, thereby confirming their subdiffusive behavior. In particular, consistent with the loci-dependent trend in MSD, the power-law fitting indicates a significant difference in the exponent values between Ori2 and Ter3. We have also plotted the MSD values with an error bar (which is the standard error; see Fig. S2 in the Supplemental Material [38]), in which the mutual differences in the mobilities of these two loci are apparent. For very short time lag $[(0.1-10)\tau_{\text{BD}}]$ MSD exponents are given by $\alpha = 0.49 \pm 0.0042$ for Ori2 and $\alpha = 0.55 \pm 0.0007$ for Ter3, which are slightly higher compared to the long time lag $[(10-100)\tau_{\text{BD}}]$ MSD exponents ($\alpha = 0.40 \pm 0.0002$ for Ori2 and $\alpha = 0.54 \pm 0.0001$ for Ter3). Experiment reports [25] that at shorter timescales, the lower and upper limit of these exponent as 0.4 and 0.5, respectively, which is in line with what we also observe from our simulations.

Together, the aforementioned observations of considerable difference in Ori2 and Ter3 movements reveal that both the loci mobility (as characterized by MSD values) and the respective values of MSD exponents are significantly dependent on the relative coordinates of these two loci. These results prompted us for a comprehensive investigation of the mobility and the diffusive exponents for thirty chromosomal loci [see Fig. 2(a) and characterize their trend. Accordingly, we calculated the MSD exponents and apparent diffusion constants from each time-averaged simulation trajectories (total $30 \times 200 = 6000$) by fitting two different lag time regions $[(0.1-10)\tau_{\text{BD}}$ and $(10-100)\tau_{\text{BD}}]$. Subsequently, we made a box plot and histogram plot for all of the loci to get a more comprehensive insight into the loci-dependent behavior of mobility. Figures 3(a) and 3(b) depict the box plot of apparent diffusion coefficient values of each of the thirty loci as a func-

tion of chromosomal coordinates, with lag time $[(0.1-10)\tau_{\text{BD}}]$ and $[(10-100)\tau_{\text{BD}}]$, respectively. From these two figures, it is evident that there are significant differences in diffusion coefficients that vary across chromosomal genomic positions in both timescales (short and long). In particular, it is also evident that among all the loci, Ori1 and Ori2 have substantially high diffusion coefficients and most of the Ter loci show lower diffusion coefficients. Figures 3(c) and 3(d) illustrate the box plot of diffusion exponents (α) of individual loci for short and long lag times, respectively. For short lag time, the median values of the exponents lie higher than $\alpha = 0.5$ and for long lag time these median values range between $\alpha = 0.4$ to $\alpha = 0.5$ for most of the loci. This results are well corroborated with experimental findings by Javer *et al.* [25], which reported that these median values lie around 0.4. In a similar fashion, Figs. 3(e) and 3(f) depict the histogram plot of MSD exponent for all trajectories of 30 loci for two different lag times. For short lag time, the mean value of the exponent $\alpha_{\text{mean}} \sim 0.502 \pm 0.067$ and for long lag time this value is lower $\alpha_{\text{mean}} \sim 0.447 \pm 0.158$. In both cases, the distribution of MSD exponent (α) values is very wide.

To understand the effect of k_0 on the loci dynamics, we have performed a fresh set of simulations for different values of $k_0 = 1.0, 100.0k_B T/\sigma^2$ and compare the results with our simulation $k_0 = 10.0k_B T/\sigma^2$. Figures S3(a) and S3(b) in the Supplemental Material [38] represent the MSD exponent and diffusion constants of the chromosomal loci for the lag time $(0.1-10)\tau_{\text{BD}}$. From these figures, it is clear that there are no dramatic changes in the dynamics of chromosomal loci with different values of k_0 and the trend of heterogeneity in loci dynamics is retained across the range of k_0 . The MSD exponents for all the loci are almost the same but the diffusion constants change. For $k_0 = 1.0k_B T/\sigma^2$, the Hi-C bonds are less stiff compared to $k_0 = 100.0k_B T/\sigma^2$. So the chromosome becomes less compact compared to $k_0 = 100.0k_B T/\sigma^2$, which escalates the values of diffusion constants.

Taken together, our Hi-C integrated computer model elucidates two key traits of *E. coli* chromosome: (a) slow subdiffusive dynamics and (b) heterogeneous chromosomal loci mobility. These results prompt us to elucidate the underlying mechanism of these features.

C. Hi-C contacts as the source of the heterogeneity in *E. coli* chromosomal diffusivity

The preceding discussions pointed out to a significant loci-coordinate-dependent subdiffusive motion of chromosome, largely consistent with the previous measurements by Javer *et al.* [25]. These experimentally consistent observations of heterogeneous mobility across chromosomal loci in our computer model demand a more microscopic physical interpretation. We noted that one of the key features of the current model, that sets it apart from other excluded-volume interaction model or other generic polymer-based “Rouse model,” is the integral presence of “Hi-C” interaction potentials to capture the experimentally obtained interbeads contact matrices. We speculated that these Hi-C contact might have a role in dictating the loci-dependent heterogeneity. Accordingly, to dissect its specific role, if any, we performed a fresh set

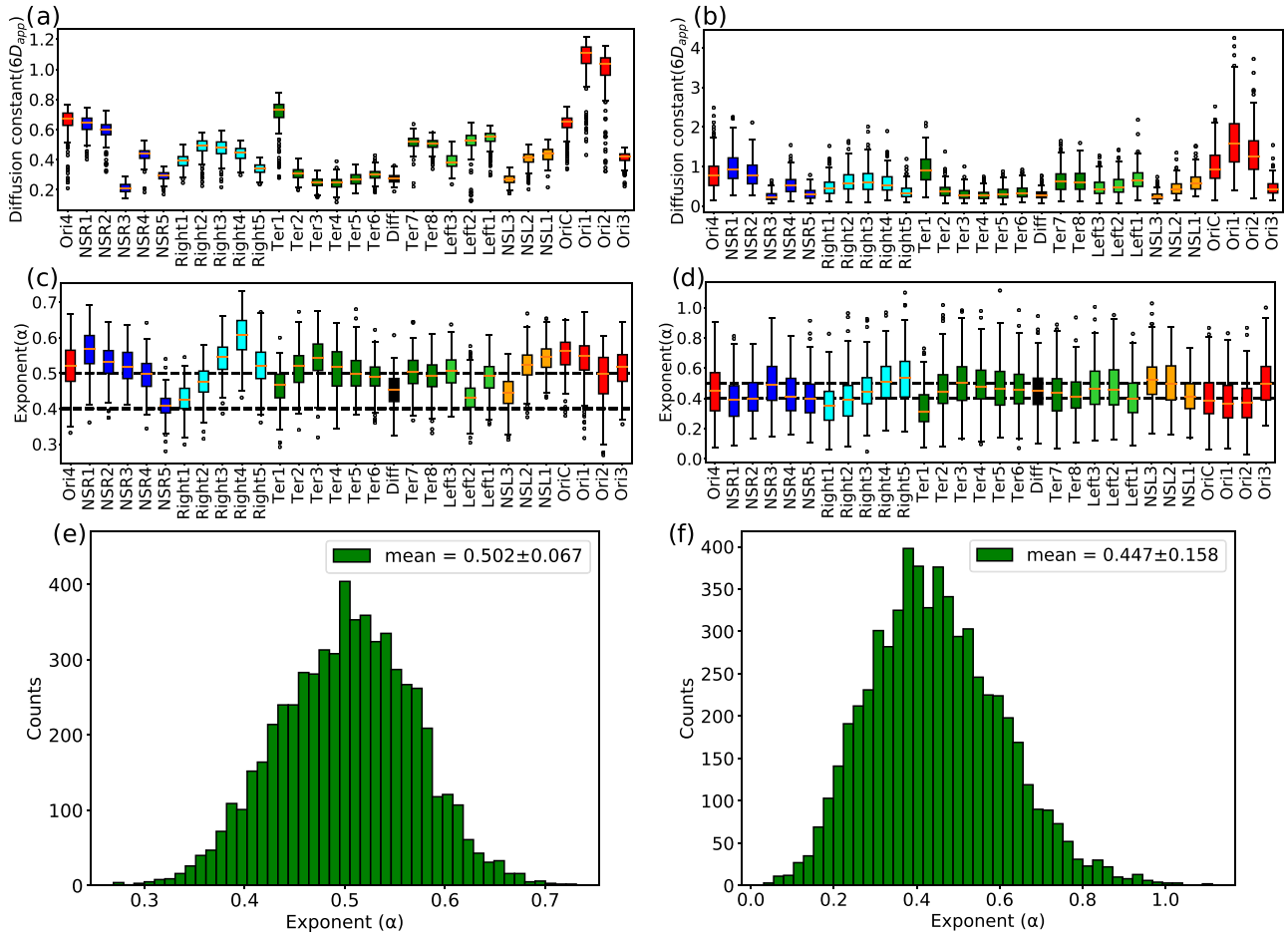


FIG. 3. Box plot of Diffusion constant as a function chromosomal loci in presence of Hi-C with lag time (a) $(0.1-10)\tau_{BD}$ and (b) $(10-100)\tau_{BD}$. In both case the value of diffusion constants vary from loci to loci, so mobility of chromosomal loci depend on their genomic coordinate. Box plot of MSD exponent for each and individual loci, by taking MSD exponent from individual trajectory of loci, with lag time (c) $(0.1-10)\tau_{BD}$ and (d) $(10-100)\tau_{BD}$. For most of the loci median values of the exponent lies higher than $\alpha = 0.5$ for short time lag and between $\alpha = 0.4$ to $\alpha = 0.5$ for long time lag, respectively. Histogram of MSD exponent by taking all of the trajectory of 30 loci [total $(200 \times 30 = 6000)$ trajectory] with lag time (e) $(0.1-10)\tau_{BD}$ and (f) $(10-100)\tau_{BD}$. From the histogram mean vale of the exponent is $\alpha_{mean} \sim 0.502 \pm 0.067$ for short time lag and $\alpha_{mean} \sim 0.447 \pm 0.158$ for long time lag, respectively.

of control dynamical simulations by removing Hi-C contacts from our computer model.

Figures 4(a) and 4(b) (red) plot the MSD exponents of all loci, as derived from the simulations trajectories of the

model in absence of Hi-C-derived interaction potential, at short and long two lag times. For the purpose of comparison, we also reproduced the MSD exponent of same set of loci as derived in simulations with Hi-C contacts [Figs. 4(a) and

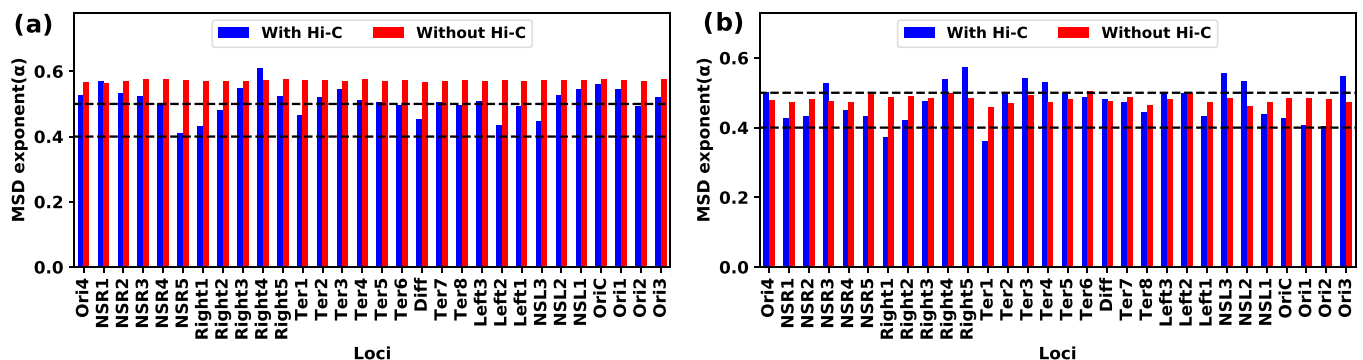


FIG. 4. Bar plot for MSD exponent as a function of chromosomal loci in presence (blue) or absence (red) of Hi-C with lag time (a) $(0.1-10)\tau_{BD}$ and (b) $(10-100)\tau_{BD}$ (red). There is a clear heterogeneity in subdiffusive exponents with respect to different loci.

4(b) (blue plots)]. The comparison indicates that the MSD exponents are uniformly similar across all loci in absence of Hi-C contacts. However, turning on these interactions in the model recapitulates the loci-dependence of MSD exponents. On a similar spirit, to investigate this loci-specific heterogeneity in diffusion coefficients, we have also calculated this diffusion constant value from simulated trajectories in the absence of Hi-C-derived interactions. Figures S4(a) and S4(b) in the Supplemental Material [38] demonstrate the apparent diffusion coefficient values as a function of chromosomal coordinates, in the absence of Hi-C-derived interactions at lag time $[(0.1-10)\tau_{BD}]$ and $[(10-100)\tau_{BD}]$, respectively. When compared with the results of simulated data in presence of Hi-C contacts (Figs. S4(c) and S4(d) in the Supplemental Material [38]), it is obvious that without Hi-C contacts, all the loci display nearly the same diffusion constant values, at two different time regions. In combination, these analysis, based on control simulations, dissect the decisive role of specific Hi-C contacts in capturing the inherent loci-dependent mobility.

The resolution of our model and the explicit incorporation of the Hi-C-derived interaction potential allowed us to track specific inter-loci contacts and pinpoint the underlying reason for the coordinate-dependent loci dynamics. In the current protocol, the intergenomic distance is modeled as inversely proportional the Hi-C contact probability ($D_{ij} = \sigma/P_{ij}$). Accordingly, the number of interbeads contacts connected to each loci gets modulated.

To get a closer insight on why Ter macrodomain demonstrates comparatively lower mobility compared to other MDs, we have computed the fraction of connections between different MDs and NS regions (total six) in our model. We have mapped the (928×928) matrix into the (6×6) matrix in accordance with their genomic coordinate and computed the fraction of mutual contacts among any pairs of MDs. Figure S5 in the Supplemental Material [38] highlights the heat map of the fraction of Hi-C contact formed within MDs and NS regions. This suggests that the fraction of intra-chromosomal connections within the Ter MD is relatively higher compared to other MDs, which slows down the mobility of Ter and its loci.

In a bid to investigate how frequent and which particular pair of chromosomal loci meet with each other for the first time, we have calculated first-passage time (FPT) for the chromosomal loci from each of the total 200 trajectories. Figures 5(a) and 5(b) compare the distribution of FPT for all the loci with all trajectories simulated with Hi-C and without Hi-C-derived interaction, respectively. In presence of Hi-C-derived interactions, numerous loci meet each other significantly more frequently for the first time compared to that in absence of Hi-C, resulting in much shorter mean first-passage time (MFPT) of $27.14\tau_{BD}$. (compared to almost double value in absence of Hi-C). More importantly, a wide distribution of FPT (with long tail) [Fig. 5(a)], evident in presence of Hi-C, reflects an inherently heterogenous, Hi-C-derived interaction-modulated encounter between the loci. Figures 5(c) and 5(d) demonstrate the network plots of FPT of chromosomal loci in presence and in absence of Hi-C, respectively, with the thickness of the lines representing the value of average FPT. The presence of nonspecificity, largely uniform encounters

between the loci is clearly evident when the Hi-C-derived interactions are turned off.

D. Tracking the origin of subdiffusive motion: Spatial and temporal coherence

Correlation functions are popular approaches, which provide dynamical insights for a system. Mathematically, velocity autocorrelation function (VAF) is defined as, $C_v^{\Delta t}(\tau) = \langle \vec{v}_i(t + \tau) \cdot \vec{v}_i(t) \rangle_t$, where angular brackets denote the time average and $v_i(t) = \frac{1}{\Delta t}(\vec{r}_i(t + \Delta t) - \vec{r}_i(t))$, Δt are the different time intervals for velocity calculation, and τ is the lag time. Physically VAF provides the strength of correlation between two velocities of the particle separated by a time interval τ . Here we have calculated an ensemble-averaged VAF for the genomic midpoint of the chromosome. Previous experimental and simulation studies on *E. coli* chromosome [21,22,48] have revealed the presence of a negative correlation peak at $\tau = \Delta t$ [49], which slowly goes to zero ($\tau \gg \Delta t$), due to the viscoelastic nature of cytoplasm and when rescaled, τ as $\tau/\Delta t$, all of the curves collapsed onto a single curve (i.e., similarity in motion). Figures 6(a) and 6(b) manifests VAF of *E. coli* chromosome for small and large time intervals (Δt), respectively. Similarly Figs. S6(a) and S6(b) in the Supplemental Material [38] show rescaled VAF for small and large time intervals (Δt). The observation of negative correlation peaks in our model is qualitatively consistent with the previous experiments and implies that our model effectively mimics a viscoelastic cytoplasm, even without explicit incorporation of viscoelasticity as well as a memory kernel [50]. We believe that the presence of long-range interbead connectivity in the form of ‘‘Hi-C’’ contacts, an essential trait of our model, is decisive in furnishing the memory and viscoelasticity in an implicit way. Instead of the genomic midpoint of the chromosome, we have also calculated VAF for Ori2 and Ter3 loci (Figs. S7(a)–S7(d) in the Supplemental Material [38]), which also show the same type of behavior.

To get a better insight into how stress is propagated between two chromosomal loci, [51,52] we have calculated the velocity-velocity correlation (VVC) function between two different chromosomal loci i and j . VVC, between two chromosomal loci i and j , is defined as $C_{vv}^{\Delta t}(\tau) = \langle \vec{v}_i(t + \tau) \cdot \vec{v}_j(t) \rangle_t$, where angular brackets denote the time average and $v_i(t) = \frac{1}{\Delta t}[\vec{r}_i(t + \Delta t) - \vec{r}_i(t)]$, Δt are the different time intervals for velocity calculation and τ is the lag time. Figures S8(a)–S8(h) in the Supplemental Material [38] demonstrate $C_{vv}^{\Delta t}(\tau)$ as a function of lag time and rescaled lag time for two different loci with increasing genomic distance, respectively. For two loci, separated by a smaller genomic distance, stress gets communicated quickly (within Δt) between each other. After that, they behave like a single loci (Figs. S8(a)–S8(f) in the Supplemental Material [38]). For loci, which are separated by larger genomic distances, stress cannot be propagated within this time interval ($\Delta t = 90\tau_{BD}$) and their motion is seen to be uncorrelated (Figs. S8(g) and S8(h) in the Supplemental Material [38]). We have also verified the scaling argument by Polovnikov *et al.* [52] with fractal globule scaling [53] that there is a timescale t^* , from which two loci become strongly coupled (Fig. S9 and Table S1 in

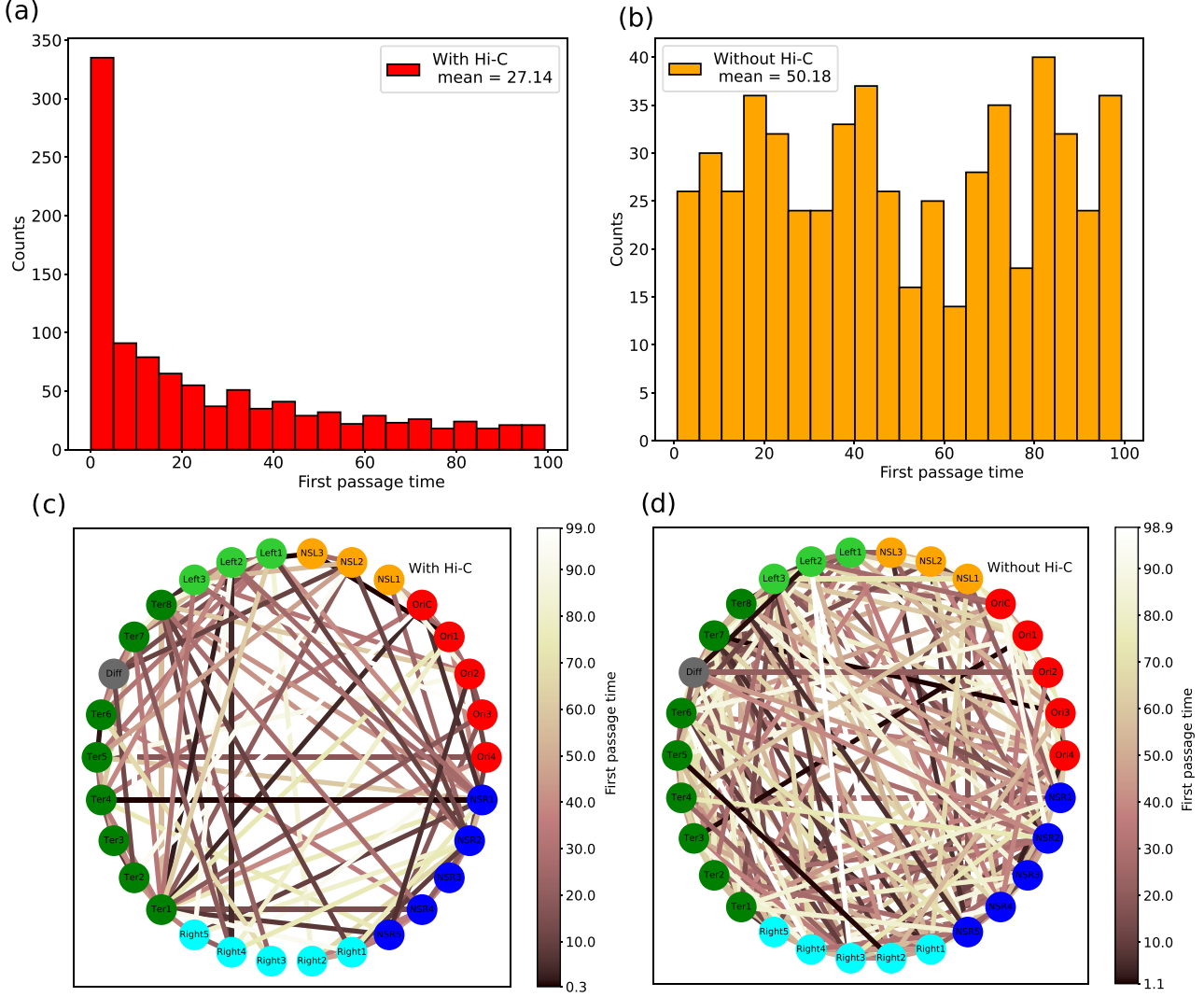


FIG. 5. (a), (b) distribution of first-passage time (FPT) with all the trajectories in the presence of Hi-C and in the absence of Hi-C, respectively. For Hi-C cases, the count of first-time meetings at a small time is very large compared to the absence of Hi-C case. (c), (d), represent the network plots of averaged FPT for different loci in presence of Hi-C and no Hi-C, respectively. Loci are denoted with different colors and placed in a circular orbit according to their genomic coordinate sequence and the connection between them represents the value-averaged FPT. Color bars are drawn with respect to the value of the averaged FPT. All length and time values are in units of σ and τ_{BD} , respectively.

the Supplemental Material [38]) and this scaling argument is more or less well corroborated with the simulations results.

Motivated by Zidovska *et al.*'s work [54], where they have used displacement correlation spectroscopy (DCS) to study spatiotemporal evolution of the global chromatin dynamics *in vivo* in nuclei of human HeLa cells, we also used the same method for spatial correlation calculation. Spatial correlation of the chromosomal loci defined as (Eq. (6) [55])

$$C_s^{\Delta t}(r) = \left\langle \frac{\sum_{i>j} [\Delta \vec{r}_i(t; \Delta t) \cdot \Delta \vec{r}_j(t; \Delta t)] \delta(r_{i,j}(t) - r)}{\sum_{i>j} \delta(r_{i,j}(t) - r)} \right\rangle_t, \quad (6)$$

where i, j are the monomer indices, and $\Delta \vec{r}_i(t; \Delta t) = \vec{r}_i(t + \Delta t) - \vec{r}_i(t)$ and Δt are the differences in time. Physically this correlation function provides the information on how the displacements of the chromosomal loci, separated by a distance

r , over time interval Δt , are correlated. Figure 6(c) shows this spatial correlation $C_s^{\Delta t}(r)$ as a function of r . As time difference Δt increases, the correlation function decays more slowly. We have also fitted $C_s^{\Delta t}(r)$ by exponentially decay function as Eq. (7):

$$f(r) = A \exp\left(-\frac{r}{\zeta}\right), \quad (7)$$

where A is a constant and ζ is the dimension of length, called correlation length (all fitting plots and parameters are given in Fig. S10 and Table S2 in the Supplemental Material [38]). Figure 6(d) demonstrates the correlation length (ζ) as a function of time difference Δt . For small values of Δt , ζ values are increasing with Δt , but for large values of Δt , ζ values are almost saturated. To quantify the spatial correlation, we have projected the displacement vector ($\Delta \vec{r}(t = 0; \Delta t)$ with $\Delta t = 1\tau_{BD}$ and $\Delta t = 90\tau_{BD}$) onto the xy plane with a

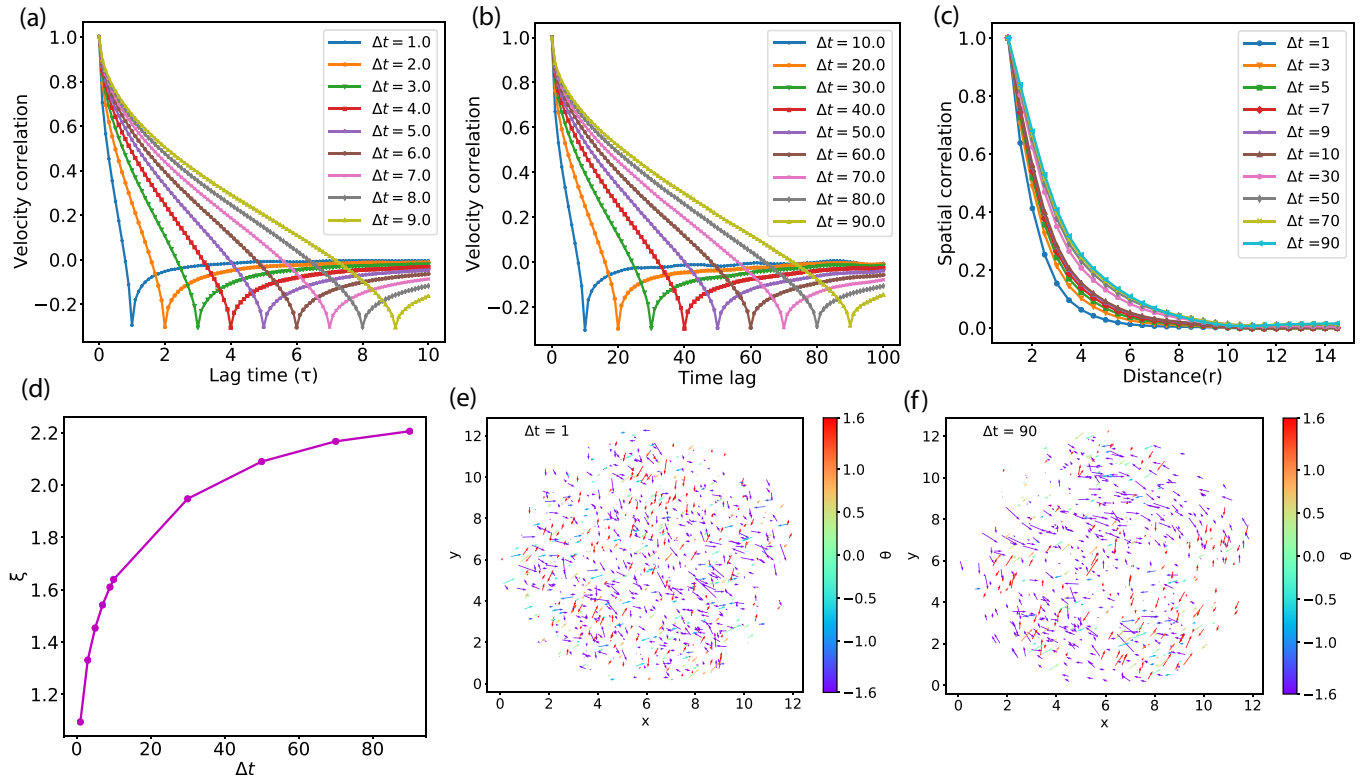


FIG. 6. Velocity autocorrelation function (VAF) as a function of lag time for different time interval (a) $\Delta t = (1.0-9.0)\tau_{BD}$ and (b) $\Delta t = (10-90)\tau_{BD}$. Both curve shows that there is a negative correlation peak at $\tau = \Delta t$ and slowly goes to zero ($\tau \gg \Delta T$), due to the viscoelastic nature of cytoplasm. (c) Spatial correlation $C_s^{\Delta t}(r)$ as a function of distance (r) for different time interval Δt . As time difference Δt increases, the correlation function decay more slowly. (d) Spatial correlation $C_s^{\Delta t}(r)$ fitted with exponentially decay function as $f(r) = A\exp(-\frac{r}{\zeta})$, where A is the constant value and ζ is correlation length. ζ increases with small values of Δt , but for large values of Δt , ζ values are almost saturated. (e) Vector field of displacement vector for time interval $\Delta t = 1$. (f) Vector field of displacement vector for time interval $\Delta t = 90$. Color bars represent the angle (θ) of the displacement vector. For a small value of time interval, Δt displacement vectors are more irregular compare to large time interval Δt . All length and time values are in units of σ and τ_{BD} , respectively.

condition ($-\sigma \leq z \leq \sigma$), and represented them by a vector field. Figures 6(e) and 6(f) depicts the vector field of displacement vector with $\Delta t = 1\tau_{BD}$ and $\Delta t = 90\tau_{BD}$, respectively. From these two figures it is clear that displacement vectors are more random for small Δt compared to large Δt , which assist to increase the correlation length with Δt .

E. The Heterogeneity in loci mobility is robust in presence of active noise

The *in vivo* cellular condition routinely involves numerous ATP-dependent biological activities (transport, metabolism) which prompts the cells to proceed far from equilibrium. A series of numerous past experiments [56–61] on eukaryotic cells and polymer model [62–65], have divulged the role of these biological active processes that initiate nonthermal fluctuations. On a related note, an important experiment by Weber *et al.* [24] has revealed that ATP-dependent fluctuation (non-thermal) control the *in vivo* dynamics of *E. coli* chromosomal loci. However, the investigation of dynamics of chromosome inside the untreated and ATP-depleted *E. coli* cells suggested that the subdiffusive scaling exponent ($\alpha_{\text{untreated}} = 0.39$, $\alpha_{\text{treated}} = 0.40$) is almost unchanged irrespective of presence or absence of ATP. However the MSD and D_{app} (apparent

diffusion coefficient) values are significantly reduced in ATP-depleted cell.

In light of present investigations' observation that chromosomal loci display a heterogeneous and coordinate-dependent mobility, we wanted to explore if this result would be replicated in presence of active noise, which is a better representative of *in vivo* environment. To introduce this into our computer model, we increased the strength of the thermal noise and performed a fresh set of dynamical simulations of the chromosome. In particular, the fluctuation dissipation theorem was accordingly changed to $\langle \vec{R}(t) \cdot \vec{R}(t') \rangle = 12D\delta(t - t')$ [55,66–68] instead of the usual expression $\langle \vec{R}(t) \cdot \vec{R}(t') \rangle = 6D\delta(t - t')$. We term our original simulations (which obey fluctuation dissipation theorem) as “passive” and current simulations (which violate fluctuation dissipation theorem) as “active.” Figures 7(a) and 7(b) show the MSD value as a function of lag time for two loci Ori2 and Ter3, respectively, with active and passive noise. From these two figures, it is evident that the MSD values of these loci are notably higher in presence of “active” noise than that of “passive” noise. A more complete comparison across all 30 loci is presented in Fig. 8. We find that the apparent diffusion constant (D_{app}) of each chromosome locus is significantly increased (almost double) in presence of “active noise” [Figs. 8(a) and 8(b)] in both short

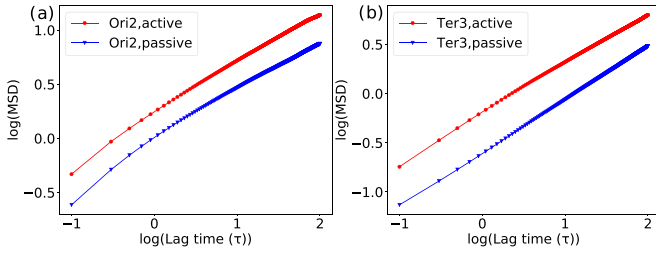


FIG. 7. (a) Log-log plot of MSD values as a function of lag time for Ori2 loci with active (red) and passive (blue) noise. (b) Log-log plot of MSD values as a function of lag time for Ter3 loci with active (red) and passive (blue) noise. MSD values of these loci are significantly different when compared with active and passive noise.

[(0.1-10) τ_{BD}] and long [(10-100) τ_{BD}] time lag, respectively. However, very interestingly, as demonstrated by Figs. 8(c) and 8(d), the respective subdiffusive exponent (α) for individual loci remains unchanged in presence of active and passive noise, at both short [(0.1-10) τ_{BD}] and long [(10-100) τ_{BD}] time lags.

For gleaning into the systematic role of noise with different strengths, we have simulated additional trajectories with noise strengths 3 and 18 along with 6 and 12. Figures S11(a) and S11(b) in the Supplemental Material [38] represent the diffusion constant for different chromosomal loci for two distinct time lag (0.1-10) τ_{BD} and (10-100) τ_{BD} . From this figure, it is clear that the diffusion constants increase remarkably with the increase of the strength of the noise. Figures S11(c) and S11(d) in the Supplemental Material [38] demonstrate the MSD exponent for different loci with two different lag times,

respectively. Interestingly, at a short lag timescale (0-10) τ_{BD} , the MSD exponents are almost the same for all the loci. But for long lag timescale (10-100) τ_{BD} , there is a small deviation in the exponents with respect to different strengths of the noise. Surprisingly, for higher strength of noise, the MSD exponents decrease for most of the loci which tells us that for a longer time the loci motions are damped. One of the possible reasons behind this is the potential interplay between noise-induced activity and the topology of the polymer chain (DNA). This noise-induced activity provides topological constraints to the DNA which damps the mobility of chromosomal loci slightly more than the passive ones at a larger lag timescale (10-100) τ_{BD} . Internal polymer topology plays a crucial role to control its spatiotemporal dynamics. DNA topoisomerases are the enzyme which are the regulator of DNA topology. They help to perform numerous functions on DNA such as unwinding, rewinding, linking, unlinking, knotting and unknotting the DNA [69-71], etc. Depending on the topological constraints of the polymer chain, various static and dynamic properties have been observed e.g. kinetically arrested state by random pinning [72,73], activity-induced polymer collapse [74], genome folding [75,76], tuning of DNA mobility [77], activity-driven topological glass transition [78-80], etc. Our observation bears resemblance with activity-driven topological glass transition in which this noise-induced activity brings various topological constraints which can be thought of in the form of effective attraction or random pinning which increases the relaxation time and escalates the system to transform to the glassy state.

Together these results indicate that due to the active noise or ATP-dependent biological activities, mobility of chromosomal loci change remarkably but subdiffusive exponents are

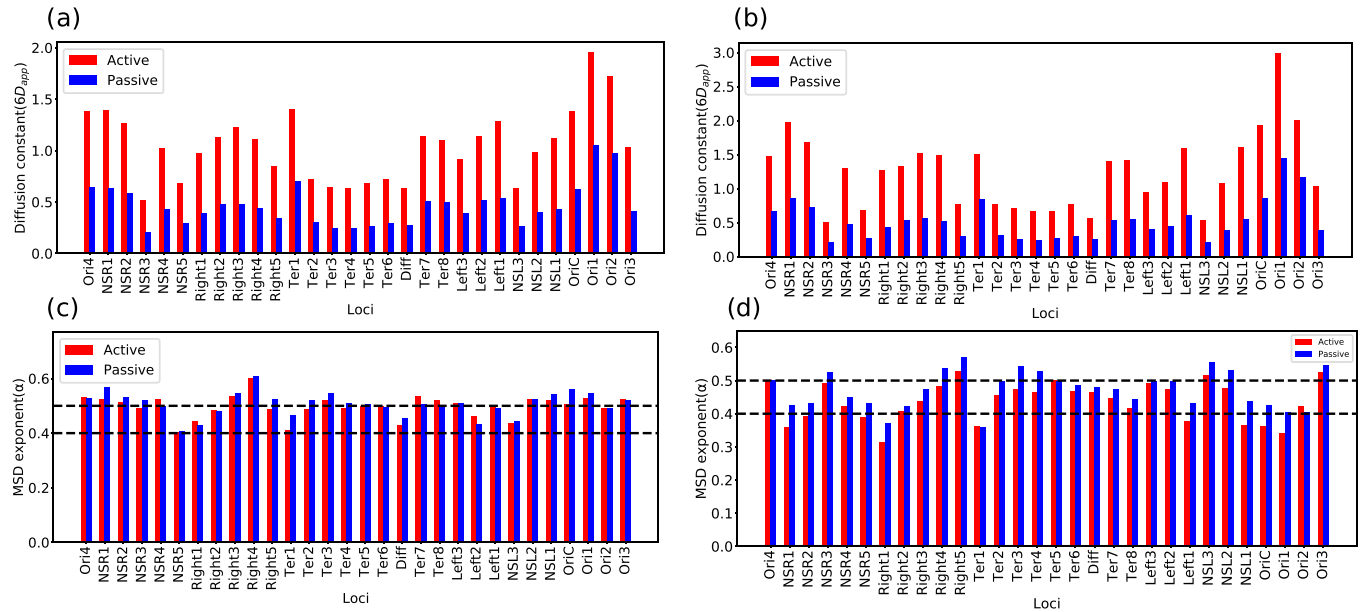


FIG. 8. (a) Bar plot of Diffusion constant as a function chromosomal loci for lag time (0.1-10) τ_{BD} in presence of active (red) and passive (blue) noise. (b) Bar plot of Diffusion constant as a function chromosomal loci for lag time (10-100) τ_{BD} in presence of active (red) and passive (blue) noise. For active case Diffusion constant is almost double as compared to the passive case. (c) Bar plot of MSD exponent as a function chromosomal loci for lag time (0.1-10) τ_{BD} in presence of active (red) and passive (blue) noise. (d) Bar plot of MSD exponent as a function chromosomal loci for lag time (10-100) τ_{BD} in presence of active (red) and passive (blue) noise. For both cases (active and passive), subdiffusive exponents are not changing significantly.

almost fixed in short lag timescale $(0.1-10)\tau_{BD}$. The observation of a robust MSD exponent irrespective of active or passive cytoplasm is consistent with previous experiment and might be due to the fact that viscoelastic nature of cytoplasm, which is effectively captured by our model's Hi-C-derived interactions, does not change notably even in presence of active noise. Nonetheless, Fig. 8 also asserts that the inherent heterogeneity and loci-dependence of the mobility and MSD exponents, as found in otherwise "passive" simulations, are rigorously preserved even in presence of "active" noise.

IV. CONCLUDING REMARKS

Our Hi-C data integrated beads-spring polymer model with Brownian dynamics simulations, reveals spatiotemporal dynamics which are consistent with previous experimental and theoretical findings on prokaryotic [21–25] chromosomal loci. We observed that chromosomal loci are moving subdiffusively but there is clear heterogeneity in subdiffusive exponents with respect to genomic coordinates as well as time. Especially Ori2 and Ter3 differ significantly in their individual displacements. The mobility of each and every loci is crucially dependent on chromosomal coordinates. We have also calculated the mean value of subdiffusive exponent by taking α value from each loci and making a histogram. The mean value is $\alpha_{\text{mean}} \sim 0.502 \pm 0.067$ for small lag time and $\alpha_{\text{mean}} \sim 0.447 \pm 0.158$ for large lag time.

To deduce the origin of the heterogeneous, coordinate-dependent diffusion, we have run a fresh set of control simulations by turning off the Hi-C-derived interaction potentials. We found that, in absence of Hi-C contacts, chromosomal loci are moving homogeneously and their mobility are unchanged with respect to genomic coordinates. This observation provides strong evidence of long-range inter-loci communications, as manifested by the "Hi-C-derived interactions," as one of key modulators of the local dynamics of the bacterial chromosome. The observation of a negative peak in velocity auto correlation function around a particular time difference ($\tau = \Delta t$) brings out the underlying viscoelastic nature effectively furnished by the Hi-C integrated model.

The origin of heterogeneous subdiffusion in the chromosomal loci can be interpreted by using arguments based on thermodynamics [81,82]. The free energy of the system can be written as $F = U - TS$ where F is the Helmholtz free energy, U is the internal energy, T is the temperature, and S is the entropy. Chromosome in absence of Hi-C-derived interaction has larger conformation entropy ($S \uparrow$) as there are no Hi-C-mediated restrictions. When we switch on Hi-C-derived interaction, the internal energy (U) of the system increases. Now for any deviation from the equilibrium position, there are penalties from the internal energy term. Accordingly, Hi-C-derived nonuniform restriction in the form of internal energy brings out nonuniform conformational entropy, which escalates the heterogeneous dynamics of chromosomal loci.

Quite gratifyingly, the subdiffusive exponents are robust with respect to active and passive noise, while the mobility of loci changes significantly in presence of active noise. This robust MSD exponent indicates that in presence of active

noise, viscoelastic nature of cytoplasm, effectively captured by our model interaction, does not change notably.

The self-organization of *E. coli* chromosome into nonoverlapping macrodomains has remained a key structural hallmark of this archetypal bacteria. However, how a domain-separated nucleoid would be influencing the dynamics of the chromosome has remained a key question for a while. This is especially complex, considering the intricacies related to segregation and the loci mobilities. In this respect, while the recent experimental demonstration of coordinate-dependent loci movements have been an intriguing discovery, underlying origin has so far been elusive. The current work brings out the importance of inter-loci encounter, statistically represented by Hi-C contacts, in dictating the heterogeneity of the local, coordinate-dependent chromosomal dynamics. The analysis of statistical encounters in the form of first-passage time of contacts (Fig. 5) and the graded extent of macrodomain-dependent fraction of contacts (Fig. S5 in the Supplemental Material [38]), provide a fair idea on how local chromosomal dynamics is governed by the long-range contacts. Overall, we feel that the current set of investigations reported in this article enriches our understanding of *E. coli*'s chromosomal dynamics, as well as the extent of information Hi-C captures.

One of the shortcomings of the current model, is that it overestimates the repulsive nature of the chromosomal loci. This causes loci which are genomically close by to have lower contact probabilities with respect to their corresponding experimental probabilities. As a future direction, one should consider using soft-core potentials which may perform better than the current hard-core repulsive potentials [83]. A further upgrade to the current model can be introduction of other macromolecules such as ribosomes and proteins into the model [84–86]. It will enable investigations into the diffusion and localization of such macromolecules [87,88] at different levels of chromosomal compaction which are brought about by multiple factors such as varying cell sizes [89], induced stress on the cell [88] and mutations. Investigations on this direction is a matter of ongoing research in our group

In the present work, we have modeled ATP-dependent nonequilibrium fluctuations by changing the fluctuation-dissipation theorem which is a very simple way to model it. Recent experimental studies [90,91] highlighted that the number and position of biomolecular condensates in bacteria can be controlled by ATP-dependent motor. In future, it would be interesting to incorporate this ATP-dependent motor in our existing model.

ACKNOWLEDGMENTS

We sincerely acknowledge Dr. V. Liroy for providing us the average cell size of the cells grown in MM at 30°C used for their study. We acknowledge the computation facilities provided by TIFR Centre for Interdisciplinary Sciences, India. We acknowledge the support of the Department of Atomic Energy, Government of India, under Project Identification No. RTI 4007 and Core Research grants provided by the Department of Science and Technology (DST) of India (CRG/2019/001219) to J.M.

- [1] G. Reshes, S. Vanounou, I. Fishov, and M. Feingold, *Phys. Biol.* **5**, 046001 (2008).
- [2] B. Volkmer and M. Heinemann, *PLoS ONE* **6**, e23126 (2011).
- [3] M. Valens, S. Penaud, M. Rossignol, F. Cornet, and F. Boccard, *EMBO J.* **23**, 4330 (2004).
- [4] O. Espeli, R. Mercier, and F. Boccard, *Mol. Microbiol.* **68**, 1418 (2008).
- [5] D. C. Grainger, D. Hurd, M. Harrison, J. Holdstock, and S. J. Busby, *Proc. Natl. Acad. Sci. USA* **102**, 17693 (2005).
- [6] R. Mercier, M.-A. Petit, S. Schbath, S. Robin, M. El Karoui, F. Boccard, and O. Espéli, *Cell* **135**, 475 (2008).
- [7] P. A. Wiggins, K. C. Cheveralls, J. S. Martin, R. Lintner, and J. Kondev, *Proc. Natl. Acad. Sci. USA* **107**, 4991 (2010).
- [8] A. Badrinarayanan, R. Reyes-Lamothe, S. Uphoff, M. C. Leake, and D. J. Sherratt, *Science* **338**, 528 (2012).
- [9] S. Bakshi, A. Siryaporn, M. Goulian, and J. C. Weisshaar, *Mol. Microbiol.* **85**, 21 (2012).
- [10] J. Dekker, K. Rippe, M. Dekker, and N. Kleckner, *Science* **295**, 1306 (2002).
- [11] J. Dostie, T. A. Richmond, R. A. Arnaout, R. R. Selzer, W. L. Lee, T. A. Honan, E. D. Rubio, A. Krumm, J. Lamb, C. Nusbaum *et al.*, *Genome Res.* **16**, 1299 (2006).
- [12] E. Lieberman-Aiden, N. L. Van Berkum, L. Williams, M. Imakaev, T. Ragozy, A. Telling, I. Amit, B. R. Lajoie, P. J. Sabo, M. O. Dorschner *et al.*, *Science* **326**, 289 (2009).
- [13] V. S. Lioy, A. Cournac, M. Marbouty, S. Duigou, J. Mozziconacci, O. Espéli, F. Boccard, and R. Koszul, *Cell* **172**, 771 (2018).
- [14] A. Wasim, A. Gupta, and J. Mondal, *Nucleic Acids Res.* **49**, 3077 (2021).
- [15] W. Sutherland, *London, Edinburgh, Dublin Philos. Mag. J. Sci.* **9**, 781 (1905).
- [16] A. Einstein, *Ann. Phys* **17**, 1 (1905).
- [17] M. Souzy, X. Yin, E. Villermaux, C. Abid, and B. Metzger, *Phys. Fluids* **27**, 041705 (2015).
- [18] J. F. Reverey, J.-H. Jeon, H. Bao, M. Leippe, R. Metzler, and C. Selhuber-Unkel, *Sci. Rep.* **5**, 11690 (2015).
- [19] A. Javer, N. J. Kuwada, Z. Long, V. G. Benza, K. D. Dorfman, P. A. Wiggins, P. Cicuta, and M. C. Lagomarsino, *Nat. Commun.* **5**, 3854 (2014).
- [20] P. Bera, A. Wasim, J. Mondal, and P. Ghosh, *Soft Matter* **17**, 7322 (2021).
- [21] S. C. Weber, A. J. Spakowitz, and J. A. Theriot, *Phys. Rev. Lett.* **104**, 238102 (2010).
- [22] S. C. Weber, J. A. Theriot, and A. J. Spakowitz, *Phys. Rev. E* **82**, 011913 (2010).
- [23] S. C. Weber, M. A. Thompson, W. E. Moerner, A. J. Spakowitz, and J. A. Theriot, *Biophys. J.* **102**, 2443 (2012).
- [24] S. C. Weber, A. J. Spakowitz, and J. A. Theriot, *Proc. Natl. Acad. Sci. USA* **109**, 7338 (2012).
- [25] A. Javer, Z. Long, E. Nugent, M. Grisi, K. Siriawetwetchakul, K. D. Dorfman, P. Cicuta, and M. C. Lagomarsino, *Nat. Commun.* **4**, 3003 (2013).
- [26] P. E. Rouse Jr., *J. Chem. Phys.* **21**, 1272 (1953).
- [27] M. Doi, S. F. Edwards, and S. F. Edwards, *The Theory of Polymer Dynamics* (Oxford University Press, Oxford, UK, 1988), Vol. 73.
- [28] M. Barbieri, M. Chotalia, J. Fraser, L.-M. Lavitas, J. Dostie, A. Pombo, and M. Nicodemi, *Proc. Natl. Acad. Sci. USA* **109**, 16173 (2012).
- [29] Y. Qi and B. Zhang, *PLoS Comput. Biol.* **15**, e1007024 (2019).
- [30] C. A. Brackley, S. Taylor, A. Papanonis, P. R. Cook, and D. Marenduzzo, *Proc. Natl. Acad. Sci. USA* **110**, E3605 (2013).
- [31] G. Shi, L. Liu, C. Hyeon, and D. Thirumalai, *Nat. Commun.* **9**, 1 (2018).
- [32] Q. MacPherson, B. Beltran, and A. J. Spakowitz, *Proc. Natl. Acad. Sci. USA* **115**, 12739 (2018).
- [33] M. A. Umbarger, E. Toro, M. A. Wright, G. J. Porreca, D. Bau, S.-H. Hong, M. J. Fero, L. J. Zhu, M. A. Marti-Renom, H. H. McAdams *et al.*, *Mol. Cell* **44**, 252 (2011).
- [34] I. Junier, F. Boccard, and O. Espeli, *Nucleic Acids Res.* **42**, 1461 (2014).
- [35] W. C. Hacker, S. Li, and A. H. Elcock, *Nucleic Acids Res.* **45**, 7541 (2017).
- [36] O. Shukron and D. Holcman, *PLoS Comput. Biol.* **13**, e1005469 (2017).
- [37] S. Saberi and E. Emberly, *PLoS Comput. Biol.* **6**, e1000986 (2010).
- [38] See Supplemental Material at <http://link.aps.org/supplemental/10.1103/PhysRevE.105.064402> for additional information. Which contains figures (S1-S11), Tables (S1-S2), and section for calculation of bead diameter and Data analysis.
- [39] T. Kalwarczyk, M. Tabaka, and R. Holyst, *Bioinformatics* **28**, 2971 (2012).
- [40] P. Swain, B. M. Mulder, and D. Chaudhuri, *Soft Matter* **15**, 2677 (2019).
- [41] M. J. Abraham, T. Murtola, R. Schulz, S. Páll, J. C. Smith, B. Hess, and E. Lindahl, *SoftwareX* **1-2**, 19 (2015).
- [42] G. Van Rossum and F. L. Drake, *Python 3 Reference Manual* (CreateSpace, Scotts Valley, CA, 2009).
- [43] J. D. Hunter, *Comput. Sci. Eng.* **9**, 90 (2007).
- [44] C. R. Harris, K. J. Millman, S. J. van der Walt, R. Gommers, P. Virtanen, D. Cournapeau, E. Wieser, J. Taylor, S. Berg, N. J. Smith *et al.*, *Nature (London)* **585**, 357 (2020).
- [45] P. Virtanen, R. Gommers, T. E. Oliphant, M. Haberland, T. Reddy, D. Cournapeau, E. Burovski, P. Peterson, W. Weckesser, J. Bright *et al.*, *Nat. Methods* **17**, 261 (2020).
- [46] A. Hagberg, P. Swart, and D. S. Chult, *Exploring Network Structure, Dynamics, and Function using NetworkX*, Tech. Rep. (Los Alamos National Laboratory, Los Alamos, NM, 2008).
- [47] W. Humphrey, A. Dalke, and K. Schulten, *J. Mol. Graph.* **14**, 33 (1996).
- [48] T. J. Lampo, N. J. Kuwada, P. A. Wiggins, and A. J. Spakowitz, *Biophys. J.* **108**, 146 (2015).
- [49] Y. Zhang and O. K. Dudko, *Annu. Rev. Biophys.* **45**, 117 (2016).
- [50] W. Deng and E. Barkai, *Phys. Rev. E* **79**, 011112 (2009).
- [51] T. J. Lampo, A. S. Kennard, and A. J. Spakowitz, *Biophys. J.* **110**, 338 (2016).
- [52] K. E. Polovnikov, M. Gherardi, M. Cosentino-Lagomarsino, and M. V. Tamm, *Phys. Rev. Lett.* **120**, 088101 (2018).
- [53] L. A. Mirny, *Chromosome Res.* **19**, 37 (2011).
- [54] A. Zidovska, D. A. Weitz, and T. J. Mitchison, *Proc. Natl. Acad. Sci. USA* **110**, 15555 (2013).
- [55] L. Liu, G. Shi, D. Thirumalai, and C. Hyeon, *PLoS Comput. Biol.* **14**, e1006617 (2018).
- [56] C. Wilhelm, *Phys. Rev. Lett.* **101**, 028101 (2008).
- [57] A. W. C. Lau, B. D. Hoffman, A. Davies, J. C. Crocker, and T. C. Lubensky, *Phys. Rev. Lett.* **91**, 198101 (2003).

- [58] F. Gallet, D. Arcizet, P. Bohec, and A. Richert, *Soft Matter* **5**, 2947 (2009).
- [59] P. Bursac, G. Lenormand, B. Fabry, M. Oliver, D. A. Weitz, V. Viasnoff, J. P. Butler, and J. J. Fredberg, *Nat. Mater.* **4**, 557 (2005).
- [60] C. P. Brangwynne, F. MacKintosh, and D. A. Weitz, *Proc. Natl. Acad. Sci. USA* **104**, 16128 (2007).
- [61] A. Caspi, R. Granek, and M. Elbaum, *Phys. Rev. Lett.* **85**, 5655 (2000).
- [62] S. Chaki and R. Chakrabarti, *J. Chem. Phys.* **150**, 094902 (2019).
- [63] N. Samanta and R. Chakrabarti, *J. Phys. A: Math. Theor.* **49**, 195601 (2016).
- [64] S. K. Anand and S. P. Singh, *Phys. Rev. E* **101**, 030501(R) (2020).
- [65] T. Eisenstecken, G. Gompper, and R. G. Winkler, *J. Chem. Phys.* **146**, 154903 (2017).
- [66] R. Bruinsma, A. Y. Grosberg, Y. Rabin, and A. Zidovska, *Biophys. J.* **106**, 1871 (2014).
- [67] J. Smrek and K. Kremer, *Phys. Rev. Lett.* **118**, 098002 (2017).
- [68] M. Bär, R. Großmann, S. Heidenreich, and F. Peruani, *Annu. Rev. Condens. Matter Phys.* **11**, 441 (2020).
- [69] Z. Liu, R. W. Deibler, H. S. Chan, and L. Zechiedrich, *Nucleic Acids Res.* **37**, 661 (2009).
- [70] C. Micheletti and E. Orlandini, *ACS Macro Lett.* **3**, 876 (2014).
- [71] S. J. McKie, K. C. Neuman, and A. Maxwell, *BioEssays* **43**, 2000286 (2021).
- [72] D. Michieletto and M. S. Turner, *Proc. Natl. Acad. Sci. USA* **113**, 5195 (2016).
- [73] W.-C. Lo and M. S. Turner, *Europhys. Lett.* **102**, 58005 (2013).
- [74] E. Locatelli, V. Bianco, and P. Maggaretti, *Phys. Rev. Lett.* **126**, 097801 (2021).
- [75] A. Rosa, *Biochem. Soc. Trans.* **41**, 612 (2013).
- [76] J. D. Halverson, J. Smrek, K. Kremer, and A. Y. Grosberg, *Rep. Prog. Phys.* **77**, 022601 (2014).
- [77] J. Smrek, J. Garamella, R. Robertson-Anderson, and D. Michieletto, *Sci. Adv.* **7**, eabf9260 (2021).
- [78] J. Smrek, I. Chubak, C. N. Likos, and K. Kremer, *Nat. Commun.* **11**, 26 (2020).
- [79] I. Chubak, C. N. Likos, K. Kremer, and J. Smrek, *Phys. Rev. Res.* **2**, 043249 (2020).
- [80] I. Chubak, S. M. Pachong, K. Kremer, C. N. Likos, and J. Smrek, *Macromolecules* **55**, 958 (2022).
- [81] W. J. Xie, Y. Qi, and B. Zhang, *PLoS Comput. Biol.* **16**, e1008262 (2020).
- [82] B. Zhang and P. G. Wolynes, *Proc. Natl. Acad. Sci. USA* **112**, 6062 (2015).
- [83] Y. Qi, A. Reyes, S. E. Johnstone, M. J. Aryee, B. E. Bernstein, and B. Zhang, *Biophys. J.* **119**, 1905 (2020).
- [84] M. Wlodarski, L. Mancini, B. Raciti, B. Sclavi, M. C. Lagomarsino, and P. Cicuta, *iScience* **23**, 101560 (2020).
- [85] S. Yu, J. Sheats, P. Cicuta, B. Sclavi, M. C. Lagomarsino, and K. D. Dorfman, *Commun. Biol.* **1**, 1 (2018).
- [86] J. Valkenburg and C. Woldringh, *J. Bacteriol.* **160**, 1151 (1984).
- [87] J. Mondal, B. P. Bratton, Y. Li, A. Yethiraj, and J. C. Weisshaar, *Biophys. J.* **100**, 2605 (2011).
- [88] Y. Zhu, S. Mohapatra, and J. C. Weisshaar, *Proc. Natl. Acad. Sci. USA* **116**, 1017 (2019).
- [89] W. T. Gray, S. K. Govers, Y. Xiang, B. R. Parry, M. Campos, S. Kim, and C. Jacobs-Wagner, *Cell* **177**, 1632 (2019).
- [90] B. Guilhas, J.-C. Walter, J. Rech, G. David, N. O. Walliser, J. Palmeri, C. Mathieu-Demaziere, A. Parmeggiani, J.-Y. Bouet, A. Le Gall *et al.*, *Mol. Cell* **79**, 293 (2020).
- [91] S. Biedzinski, B. Parmar, and S. C. Weber, *Mol. Cell* **79**, 205 (2020).